

Detecting Adversarial Perturbations in Multi-Task Perception

Marvin Klingner¹, Varun Ravi Kumar² Senthil Yogamani², Andreas Bär¹, and Tim Fingscheidt¹

Abstract—While deep neural networks (DNNs) achieve impressive performance on environment perception tasks, their sensitivity to adversarial perturbations limits their use in practical applications. In this paper, we (i) propose a novel adversarial perturbation detection scheme based on multi-task perception of complex vision tasks (i.e., depth estimation and semantic segmentation). Specifically, adversarial perturbations are detected by inconsistencies between extracted edges of the input image, the depth output, and the segmentation output. To further improve this technique, we (ii) develop a novel edge consistency loss between all three modalities, thereby improving their initial consistency which in turn supports our detection scheme. We verify our detection scheme’s effectiveness by employing various known attacks and image noises. In addition, we (iii) develop a multi-task adversarial attack, aiming at fooling both tasks as well as our detection scheme. Experimental evaluation on the Cityscapes and KITTI datasets shows that under an assumption of a 5% false positive rate up to 100% of images are correctly detected as adversarially perturbed, depending on the strength of the perturbation. Code will be available on github. A short video at <https://youtu.be/KKa6gOyWmH4> provides qualitative results.

I. INTRODUCTION

Robustness of Deep Neural Networks: Deep neural networks achieve impressive performance on semantic segmentation [1], [2], depth estimation [3], [4], [5], [6], [7], [8], object detection [9], [10], soiling detection [11], [12], moving object detection [13] or pose estimation [14], [15], [16]. However, recent research has shown that visually imperceptible perturbations exist [17], [18] and lead to performance drops (cf. Fig. 1). At the latest since the discovery of universal adversarial perturbations [19], [20], generalizing across images and networks, it is clear that such perturbations present a significant risk in safety-critical applications including autonomous driving or augmented reality. While most works on adversarial perturbations focus on image classification [17], [18], we address the less explored tasks of depth estimation and semantic segmentation [21], which are essential elements of an environment perception.

Detecting Adversarial Perturbations: As a result of adversarial perturbations’ discovery many works emerged, proposing defenses [22], [23], as well as circumventing those defenses [24]. While defense approaches are able to mitigate the effect of smaller perturbations, larger perturbations still pose a challenge, motivating the use of adversarial perturbation detection methods [25], [26], [27]. These methods do not prevent the (catastrophic) effects of the perturbation, but

¹Marvin Klingner, Andreas Bär, and Tim Fingscheidt are with the Institute for Communications Technology, Technische Universität Braunschweig, Schleinitzstr. 22, 38106 Braunschweig, Germany {m.klingner, andreas.baer, t.fingscheidt}@tu-bs.de

²Varun Ravi Kumar and Senthil Yogamani are with Valeo.

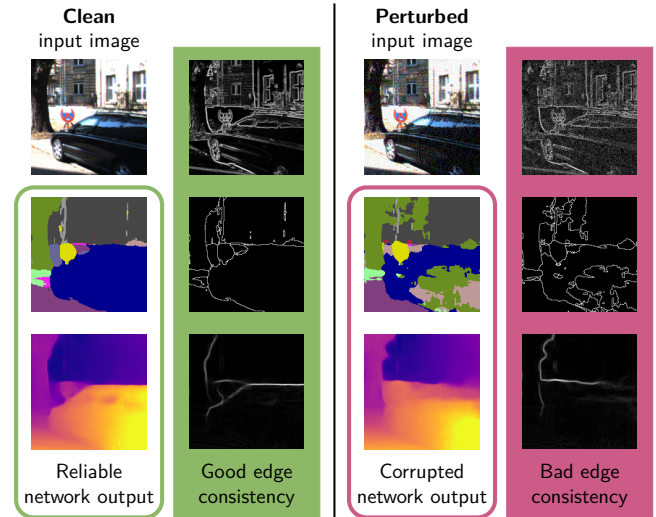


Fig. 1: **General concept** of our detection framework. Left-right pairs of input images and edges (top row), segmentation outputs and edges (middle row), and depth outputs and edges (bottom row) are depicted. A clean input image (left half) has consistent edges with the depth and segmentation network outputs. If the input image is perturbed (right half), significantly reduced input-output and output-output edge consistencies can be observed.

rather indicate the existence of a perturbation on the image. Thereby, subsequent systems can be made aware that the network output is not reliable (cf. Fig. 1) and take measures accordingly. Note that current works in this field focus on image classification [25], [26], [27], while we address the underrepresented tasks of semantic segmentation [28] and depth estimation [29]. Compared to works on image classification, we make use of the more complex output structure of these tasks, i.e., we utilize the edge consistency between the input image and the network outputs (cf. Fig. 1). Also, our detector can be appended to a given multi-task DNN in a straightforward manner, while other approaches rely on quite complex approaches with additional detection networks [25], [26], [27], or network ensembles [28].

Adversarial Perturbations for Multi-Task Networks: Environment perception systems are often implemented as a multi-task network, trained by multi-task learning, due to the advantages in terms of performance and efficiency [30]. Regarding adversarial perturbations, Mao et al. [29] have shown that multi-task learning strengthens adversarial robustness due to the increased difficulty of successfully attacking several tasks. Subsequent works aimed in similar directions in exploring different task combinations [31], [32], [33], [34], [35], comparing the effectiveness of adding different auxiliary tasks [36], or studying the relatedness of tasks

by the generalizability of adversarial perturbations across them [37], [38]. While the positive effects on adversarial *robustness* are quite well explored, our work is the first to propose an adversarial perturbation *detection* based on multi-task learning of two complex vision tasks, in our case, semantic segmentation and depth estimation.

Contributions: In this work, we propose an adversarial perturbation detection mechanism based on edge extraction from the input image, the semantic segmentation output, as well as from the depth output. By comparing their edge consistency as shown in Fig. 1, we can distinguish clean images with good edge consistency from perturbed images with rather bad edge consistency. Prior works have shown the benefit of enforcing edge consistency on the prediction performance of a multi-task network [39], [40], however, to the best of our knowledge, we are the first to use edge consistency both as loss and metric for adversarial perturbation detection. Specifically, our contributions are as follows: First, we address adversarial perturbation detection for the tasks of depth estimation and semantic segmentation. Second, we propose a detection method based on edge consistencies of a multi-task network. Third, we propose a consistency loss function to further support our detection method. Fourth, we verify our detection method against an attacker with white-box knowledge of both the multi-task network *and* our detection method. Finally, we show the effectiveness of our detection method against several adversarial attacks, in particular the Orthogonal-PGD (O-PGD) attack [41] that recently fooled most state-of-the-art adversarial perturbation detection methods on the image classification task.

II. TRAINING AND DETECTION METHOD DESCRIPTION

In this section we outline our edge-consistent multi-task learning (MTL) framework (cf. Fig. 2) as well as our adversarial perturbation detection method (cf. Fig. 3).

A. Edge-Consistent Multi-Task Learning Framework

In the following, we describe our multi-task learning setup. In contrast to prior works, we specifically aim at a high edge consistency to support our adversarial perturbation detection.

Multi-Task Learning Setup: For joint estimation of depth and segmentation we employ a single encoder and two task-specific decoders as shown in Fig. 2. The input to our network is a single RGB image $\mathbf{x}_t = (x_{t,i,c}) \in \mathbb{I}^{H \times W \times C}$ at time instance t with height H , width W , $C = 3$ color channels, and pixel position $i \in \mathcal{I} = \{1, \dots, H \cdot W\}$ normalized to the range $\mathbb{I} = [0, 1]$. The segmentation decoder outputs class probabilities $\mathbf{y}_t = (y_{t,i,s}) \in \mathbb{I}^{H \times W \times |\mathcal{S}|}$ for $|\mathcal{S}|$ semantic classes. The class probabilities are normalized pixel-wise over the set of classes $\mathcal{S} = \{1, \dots, |\mathcal{S}|\}$ such that $\sum_{s \in \mathcal{S}} y_{t,i,s} = 1$. Accordingly, the final classes $\mathbf{m}_t = (m_{t,i}) \in \mathcal{S}^{H \times W}$ can be obtained pixel-wise by $m_{t,i} = \operatorname{argmax}_{s \in \mathcal{S}} y_{t,i,s}$. The depth decoder outputs a depth map $\mathbf{d}_t = (d_{t,i}) \in \mathbb{D}^{H \times W}$ with pixel-wise depth values $d_{t,i}$ in the pre-defined depth range $\mathbb{D} = [d^{\min}, d^{\max}]$ with lower bound d^{\min} and upper bound d^{\max} . The network is

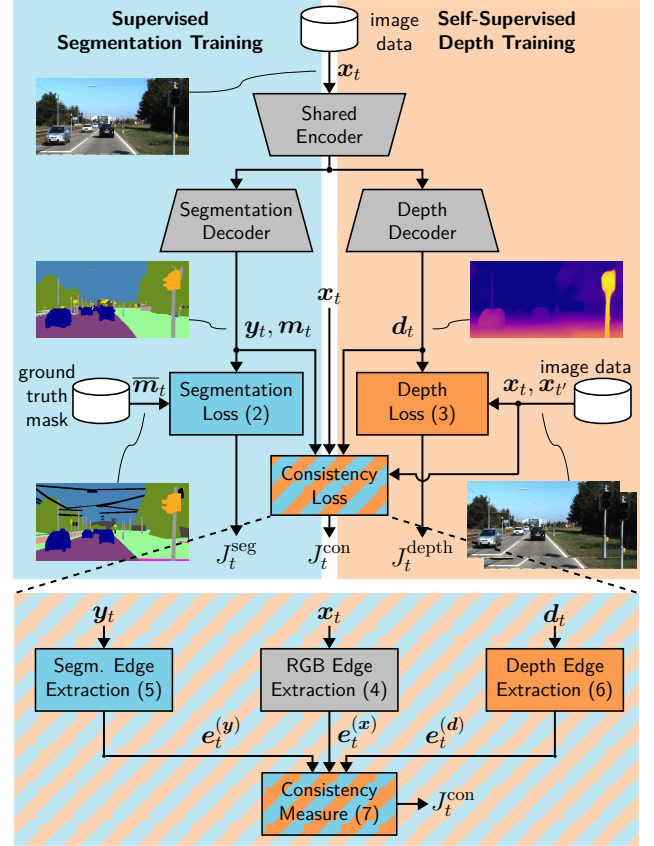


Fig. 2: **Edge-consistent multi-task training framework:** The single tasks of the multi-task network are trained by their task-respective losses. Additionally, we apply our edge-consistency loss between the RGB image and the network outputs.

trained using task-specific losses J^{depth} and J^{seg} for depth and segmentation, respectively, as well as our novel edge consistency loss J^{con} , yielding the total loss

$$J^{\text{tot}} = J^{\text{seg}} + J^{\text{depth}} + \mu J^{\text{con}}. \quad (1)$$

While μ regularizes the influence of the edge consistency loss, the influence of the single tasks is weighted by a gradient weighting factor $\lambda = 0.1$ in the encoder [42], [43].

Semantic Segmentation Training: We train the semantic segmentation using ground truth labels $\bar{\mathbf{m}}_t = (\bar{m}_{t,i}) \in \mathcal{S}^{H \times W}$. We use them in a one-hot encoded fashion as $\bar{\mathbf{y}}_t = (\bar{y}_{t,i,s}) \in \{0, 1\}^{H \times W \times |\mathcal{S}|}$, such that $\bar{m}_{t,i} = \operatorname{argmax}_{s \in \mathcal{S}} \bar{y}_{t,i,s}$. We apply a class-balanced cross-entropy loss

$$J^{\text{seg}} = -\frac{1}{|\mathcal{I}|} \sum_{i \in \mathcal{I}} \sum_{s \in \mathcal{S}} w_s \bar{y}_{t,i,s} \cdot \log(y_{t,i,s}), \quad (2)$$

between ground truth $\bar{\mathbf{y}}_t$ and prediction \mathbf{y}_t where the class weights w_s are computed according to [44] and $|\mathcal{I}| = H \cdot W$.

Depth Estimation Training: We train the depth estimation in a self-supervised fashion on monocular videos [45] according to recent state-of-the-art approaches [4], [43]. Here, the depth estimation problem is reformulated to an image reprojection between pairs of consecutive images (\mathbf{x}_t ,

$\mathbf{x}_{t'}$) with $t' \in \mathcal{T}' = \{t-1, t+1\}$. First, the pixel coordinates of the image \mathbf{x}_t are projected into a point cloud using the depth output \mathbf{d}_t . Afterwards, the point cloud is projected onto the pixel coordinates of the image $\mathbf{x}_{t'}$, where the RGB values $\mathbf{x}_{t'}$ are sampled such that a projected image $\mathbf{x}_{t' \rightarrow t}$ is generated. For more details, we refer to [43].

As a consequence, the depth output \mathbf{d}_t can be optimized by minimizing the projection error for the generation of $\mathbf{x}_{t' \rightarrow t}$ by calculating its difference to the actual image \mathbf{x}_t as

$$J_t^{\text{depth}} = \frac{1}{|\mathcal{I}|} \sum_{i \in \mathcal{I}} \min_{t' \in \mathcal{T}'} \left(\frac{\alpha}{2} (1 - \text{SSIM}_i(\mathbf{x}_t, \mathbf{x}_{t' \rightarrow t})) + (1 - \alpha) \frac{1}{C} \|\mathbf{x}_{t,i} - \mathbf{x}_{t' \rightarrow t,i}\|_1 \right), \quad (3)$$

where a mixture of two differences is used: The structural similarity (SSIM) difference $\text{SSIM}_i(\cdot) \in \mathbb{I}$, where we adopt the efficient implementation from [4] in computing this difference on 3×3 patches around the pixel index i , and the absolute difference $\|\cdot\|_1$, computed over all $C = 3$ color channels at pixel index i . Both losses are weighted by a factor $\alpha = 0.85$ as in prior art [4], [43] and a pixel-wise minimum is applied to handle occlusions. We further employ the auto-masking technique from [4] to handle static frames.

Novel Edge-Consistency Training: As we detect adversarial perturbations by low edge consistency of network input and outputs, we aim at increasing the edge consistency between them on unperturbed images by a newly introduced edge consistency loss. In contrast to prior works in multi-task learning we do not only enforce edge consistency between the network outputs [40] but also between input and both outputs. Specifically, we apply edge consistency losses between the three pairs $(k, \kappa) \in \mathcal{K} = \{(\mathbf{y}, \mathbf{x}), (\mathbf{x}, \mathbf{d}), (\mathbf{y}, \mathbf{d})\}$. As a first step, we extract their edges. For the RGB image, we extract edges for pixel position i as

$$\mathbf{e}_{t,i}^{(\mathbf{x})} = (e_{t,i,n}^{(\mathbf{x})}) = \left(\frac{1}{C} \|\partial_h \mathbf{x}_{t,i}\|_1, \frac{1}{C} \|\partial_w \mathbf{x}_{t,i}\|_1 \right) \in \mathbb{R}_+^2, \quad (4)$$

by calculating the gradients (i.e., the value difference) ∂_n between neighboring pixels in height ($n = h$) and width dimension ($n = w$). Similarly, the segmentation edges

$$\mathbf{e}_{t,i}^{(\mathbf{y})} = (e_{t,i,n}^{(\mathbf{y})}) = \left(\frac{1}{|\mathcal{S}|} \|\partial_h \mathbf{y}_{t,i}\|_1, \frac{1}{|\mathcal{S}|} \|\partial_w \mathbf{y}_{t,i}\|_1 \right) \in \mathbb{R}_+^2, \quad (5)$$

are obtained from the class probabilities \mathbf{y}_t as the actual segmentation map \mathbf{m}_t is obtained by a non-differentiable argmax operation and can therefore not be used during training. For the depth output, we extract edges

$$\mathbf{e}_{t,i}^{(\mathbf{d})} = (e_{t,i,n}^{(\mathbf{d})}) = (|\partial_h \tilde{\eta}_{t,i}|, |\partial_w \tilde{\eta}_{t,i}|) \in \mathbb{R}_+^2 \quad (6)$$

from the mean-normalized inverse depth $\tilde{\eta}_t \in \mathbb{R}^{H \times W}$, whose elements are computed by $\tilde{\eta}_{t,i} = \frac{\eta_{t,i}}{HW \sum_{j \in \mathcal{I}} \eta_{t,j}}$ with $\eta_{t,i} = \frac{1}{d_{t,i}}$, as previous works usually use this formulation when using a first-order depth gradient in a loss function [4], [46].

Our proposed edge-consistency loss encourages edges of modality κ at pixels i to be structurally similar to edges of

modality k which we achieve using the SSIM difference as

$$J_t^{\text{con}} = 1 - \frac{1}{6|\mathcal{I}|} \sum_{i \in \mathcal{I}} \sum_{(k, \kappa) \in \mathcal{K}} \sum_{n \in \{h, w\}} \text{SSIM}_i(e_{t,n}^{(\kappa)}, e_{t,n}^{(k)}). \quad (7)$$

We average over the SSIM difference of 3×3 patches around pixel index $i \in \mathcal{I}$, modality pairs $(k, \kappa) \in \mathcal{K}$, and gradient directions $n \in \{h, w\}$ (cf. (4), (5), and (6)). In other words, (7) can be interpreted in a way that segmentation and depth edges are encouraged at pixels with high RGB value gradients and depth edges are further encouraged in regions with high segmentation class probability gradients. Note that our loss function may not be optimal for performance due to shadows or textures (in which neither depth nor segmentation edges are desired) but it rather aims at a high edge consistency to facilitate a more rapid consistency disturbance by adversarial perturbations.

B. Adversarial Perturbation Detection by Edge Consistency

The aim of our adversarial perturbation detection method depicted in Fig. 3 is to detect input perturbations $\mathbf{r}_\epsilon \in [-1, 1]^{H \times W \times C}$ of strength $\epsilon = \sqrt{\frac{1}{HW C} \mathbb{E}(\|\mathbf{r}_\epsilon\|_2^2)}$ (defined by the expectation value of the sum of the squared noise pixels) on an input image \mathbf{x}_t , see also [31]. The perturbation is added, yielding the perturbed image

$$\mathbf{x}_{t,\epsilon} = \mathbf{x}_t + \mathbf{r}_{t,\epsilon}. \quad (8)$$

For simplicity and consistency to Sec. II-A, we will omit the index ϵ in the following, i.e., $\mathbf{x}_{t,\epsilon} \hat{=} \mathbf{x}_t$.

Edge Consistency Calculation: As shown in Fig. 3, the inputs to our detection method are the (perturbed) input image \mathbf{x}_t , the depth output \mathbf{d}_t , and the segmentation output \mathbf{m}_t . As a first step, we extract the edges of all three modalities. The RGB image edges and the depth edges are extracted according to (4) and (6), respectively. Regarding the segmentation map, an edge is simply defined as two neighboring pixels containing different classes. Accordingly, the segmentation edges $\mathbf{e}_t^{(\mathbf{m})}$ are computed by

$$\mathbf{e}_{t,i}^{(\mathbf{m})} = ([|\partial_h m_{t,i}| > 0], [|\partial_w m_{t,i}| > 0]) \in \{0, 1\}^2 \quad (9)$$

where $[\cdot]$ is the Iverson bracket, which yields 1, if the condition in the bracket is true, and 0 otherwise. We then calculate three pairwise consistencies between $\mathbf{e}_t^{(k)}, \mathbf{e}_t^{(\kappa)}$ with $(k, \kappa) \in \mathcal{K}' = \{(\mathbf{m}, \mathbf{x}), (\mathbf{x}, \mathbf{d}), (\mathbf{m}, \mathbf{d})\}$ using the SSIM metric defined in [47], yielding the edge consistencies $\text{SSIM}_t^{(k, \kappa)} = \text{SSIM}(\mathbf{e}_t^{(k)}, \mathbf{e}_t^{(\kappa)})$ as shown in the top left part of Fig. 3. Note that in contrast to the edge-consistency loss, the structural similarities $\text{SSIM}_t^{(k, \kappa)}$ of the detector are computed according to the original formulation [47], and in non-differentiable fashion because the segmentation map \mathbf{m}_t is computed using the argmax operation, making a direct calculation of adversarial perturbations impossible.

Detection Generation: To generate a detection score $z_t^{(k, \kappa)}$, denoting whether an input image is adversarially perturbed, we further rely on a threshold $\theta^{(k, \kappa)}$ (cf. bottom left part in Fig. 3). This threshold is obtained from the distribution of consistencies on the validation set where images are

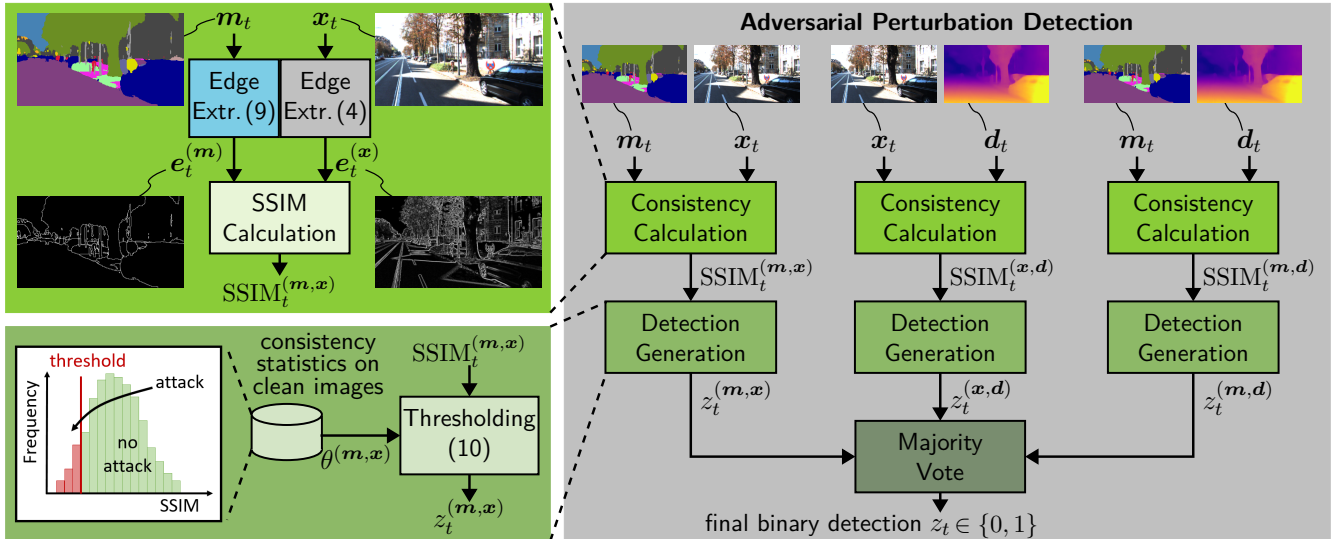


Fig. 3: **Overview of our adversarial perturbation detection method** for semantic segmentation and depth estimation. We first calculate the three edge consistencies $SSIM_t^{(k,\kappa)}$ pairwise between the (perturbed) input image, the depth output and the segmentation output. Afterwards, the binary detection output is generated by comparing any of the three edge consistencies to a threshold $\theta^{(k,\kappa)}$. The final detection output is created by majority vote.

known to be unperturbed. We choose the threshold such that a fraction $\gamma \in [0, 1]$ of consistencies is below the threshold. If $\gamma = 0$, the detector never wrongfully classifies clean images as perturbed. If the edge consistency is below the threshold $\theta^{(k,\kappa)}$, it indicates the presence of an adversarial perturbation. Mathematically, the detection result $z_t^{(k,\kappa)}$ is obtained as

$$z_t^{(k,\kappa)} = [\text{SSIM}(e_t^{(k)}, e_t^{(\kappa)}) < \theta^{(k,\kappa)}], \quad (10)$$

where $[\cdot]$ again represents the Iverson bracket. The final detection z_t is generated by using a majority vote of the three single detections $z_t^{(m,x)}$, $z_t^{(x,d)}$, and $z_t^{(m,d)}$ as shown in the bottom right part of Fig. 3.

C. Multi-Task Adversarial Attack Design

The aim of an untargeted adversarial attack is to optimize the perturbation $r_{t,\epsilon}$ in (8) to minimize the prediction performance of a DNN. Accordingly, the negative impact of an adversarial perturbation is usually stronger compared to random perturbations. For an in-depth overview we report on Gaussian noise or salt and pepper (S&P) noise, representing random perturbations, and on FGSM [17], BIM [18], PGD [23], and O-PGD [41], representing adversarial perturbations. We apply all attacks with the standard settings reported in the respective publications.

Adversarial Perturbation Calculation: In the following, we specify a new attack aiming at fooling both modalities of our multi-task perception as well as our detection method. We exemplarily describe its calculation for the FGSM adversarial attack [17], while its extension to more complex attacks is achieved straightforward by the iterative computation protocol used in such attacks.

For the FGSM attack, the perturbation is calculated by

$$r_{t,\epsilon} = \epsilon \cdot \text{sign}(\nabla_x J_t^{\text{adv}}), \quad (11)$$

where we calculate the derivative ∇_x of our adversarial perturbation loss function J_t^{adv} with respect to the input

image x and apply element-wise the signum function $\text{sign}(\cdot)$. Accordingly, the adversarial perturbation $r_{t,\epsilon}$ is optimized to maximize J_t^{adv} by (11). While previous works usually optimize attacks for a single task, we aim at fooling both tasks of the multi-task network by setting

$$J_t^{\text{adv}} = J_t^{\text{depth}} + J_t^{\text{seg}}, \quad (12)$$

with J_t^{depth} and J_t^{seg} computed according to (3) and (2), respectively. Maximizing (12) by (11) naturally aims at a decreased performance of the multi-task network.

Incorporating the Detection Method: If the attacker calculating the adversarial perturbation $r_{t,\epsilon}$ has knowledge about the detection, he could additionally aim at fooling the detection method. As our detection relies on inconsistency between input and outputs, the attacker could additionally aim at achieving a high edge consistency, characterized by a low edge consistency loss J_t^{con} (7). Accordingly, the adversarial perturbation loss can be written as

$$J_t^{\text{adv}} = J_t^{\text{depth}} + J_t^{\text{seg}} - \tilde{\mu} J_t^{\text{con}}, \quad (13)$$

where $\tilde{\mu}$ is a loss weighting factor. This objective is difficult to solve for an attacker, as optimizing the adversarial perturbation $r_{t,\epsilon}$ towards a better consistency during one training step may make the image $x_{t,\epsilon}$ (cf. (8)) inconsistent to the outputs of the subsequent training step.

III. IMPLEMENTATION DETAILS

Here, we describe our used datasets, evaluation metrics, network architecture, and multi-task training details to facilitate reproducibility. We employ the PyTorch library [51] executed on an NVIDIA Tesla P100 graphics card.

Datasets: We use the well-established benchmark datasets KITTI [52] and Cityscapes [53]. The KITTI dataset is generally used to benchmark depth estimation models. We utilize the 29,000 images defined by [48] as well as 200

TABLE I: **Prediction performance ablation and comparison to baselines** on the KITTI-2015 validation set. We show the performance on the depth and segmentation tasks as well as the consistency between the RGB input image and the depth and segmentation outputs. We compare the segmentation and the depth single-task models, a multi-task (MT) model, a model trained with an additional smoothness loss [48], models trained with our edge consistency loss (ECL) (7) but only one pair being evaluated: $(k, \kappa) = (\mathbf{y}, \mathbf{x})$ or $(k, \kappa) = (\mathbf{x}, \mathbf{d})$ or $(k, \kappa) = (\mathbf{y}, \mathbf{d})$, and finally our proposed model trained with the full ECL of (7) (**Ours**). Best results are printed in boldface, second-best are underlined.

Method	Segmentation	Depth							Consistency		
	mIoU [%] \uparrow	Abs Rel \downarrow	Sq Rel \downarrow	RMSE \downarrow	RMSE log \downarrow	$\delta < 1.25 \uparrow$	$\delta < 1.25^2 \uparrow$	$\delta < 1.25^3 \uparrow$	$\overline{\text{SSIM}}^{(m,x)} \uparrow$	$\overline{\text{SSIM}}^{(x,d)} \uparrow$	$\overline{\text{SSIM}}^{(m,d)} \uparrow$
EPC [49]	-	0.131	1.254	6.117	0.220	0.826	0.931	0.973	-	-	-
UnRigidFlow [50]	-	0.108	1.020	5.528	0.195	0.863	0.948	0.980	-	-	-
SGDepth [43]	50.1	0.097	0.983	6.173	0.160	0.898	0.972	0.990	-	-	-
only segmentation	45.2	-	-	-	-	-	-	-	-	-	-
only depth	-	0.107	1.082	6.470	0.173	0.878	0.967	0.988	-	-	-
Ours w/o ECL = MT	50.1	<u>0.099</u>	<u>0.992</u>	6.219	<u>0.162</u>	<u>0.894</u>	0.971	0.990	<u>0.20</u>	0.34	0.41
MT + smooth [48]	47.4	0.101	0.997	6.125	0.163	0.893	0.972	0.990	<u>0.20</u>	0.34	0.43
MT + ECL(\mathbf{y}, \mathbf{x})	48.8	0.102	1.037	6.149	0.163	<u>0.894</u>	0.973	0.990	<u>0.20</u>	0.34	<u>0.44</u>
MT + ECL(\mathbf{x}, \mathbf{d})	<u>51.1</u>	0.106	1.109	6.285	0.168	0.885	0.971	0.990	<u>0.20</u>	0.52	0.24
MT + ECL(\mathbf{y}, \mathbf{d})	48.5	0.103	1.034	6.178	0.164	0.891	0.971	0.990	<u>0.20</u>	0.33	0.50
Ours	51.6	0.101	1.030	<u>6.137</u>	<u>0.162</u>	<u>0.894</u>	<u>0.972</u>	0.990	0.21	<u>0.36</u>	<u>0.44</u>

images from the KITTI-2015 dataset [54] for validation. On the other hand, the Cityscapes dataset is generally used to benchmark semantic segmentation models for urban scene understanding. It contains well-defined splits of 2,975 and 500 images for training and validation, respectively. We took design decisions regarding our detection method on the KITTI dataset (cf. Table II), subsequently testing it without any changes on both KITTI and Cityscapes to verify our method’s generalizability.

Evaluation Metrics: We evaluate the semantic segmentation task using the mean intersection over union (mIoU) metric as defined in [55]. For the depth estimation task, we use the commonly reported four error metrics as well as three accuracy metrics as defined in [3]. To evaluate our detection method, we follow common practices¹ in using the detection success rate $\text{TPR}_{5\%}$ (true positive rate) while fixing the false positive rate (FPR) on clean images to 5% through the thresholds $\theta^{(k,\kappa)}$ (cf. Sec. II-B). We additionally report the prediction performance of the multi-task DNN under perturbations, which is also of interest, since a high detection rate is only important at a low prediction performance.

Network Architecture: We employ an encoder-decoder architecture with a ResNet-18 encoder [56] and task-specific decoders for the depth and segmentation tasks adopted from [43]. The decoders utilize a fully convolutional architecture, where features from the encoder are concatenated with decoder features and subsequently passed through two convolutional layers and nearest neighbor upsampling. The depth output is computed at four resolutions as a sigmoid output $\sigma_t = (\sigma_{t,i})$. The depth map is then obtained by $\frac{1}{a\sigma_{t,i}+b}$, where a and b constrain the depth to the range $[0.1, 100]$. The segmentation output is computed only at the highest resolution by applying a softmax function to the $|\mathcal{S}|$ output feature maps.

Multi-Task Training Details: Our multi-task network is trained simultaneously by employing the Cityscapes training set for the segmentation task and the KITTI training set for

the depth estimation task. In each training step, we use mixed batches with 6 images from each dataset, i.e., in total 12 images in each batch. All images are processed by the multi-task network, while the losses are only applied on the task-specific images. We train all networks for 40 epochs using the Adam optimizer [57] with a learning rate of 10^{-4} , which is reduced to 10^{-5} after 30 epochs.

IV. EXPERIMENTAL EVALUATION

In this section, we first analyze the effect of different aspects of our edge-consistent multi-task training. Afterwards, we give insights into the design of our detection method by an ablation study. Finally, we evaluate our method’s effectiveness against random and adversarial perturbations.

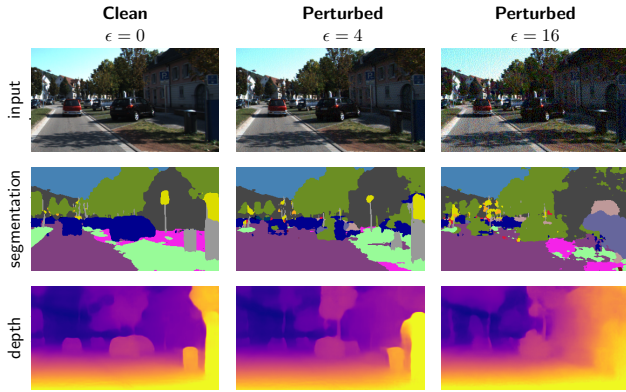
A. Prediction Performance

In Table I, we evaluate the prediction performance of our method on the KITTI-2015 dataset as it is well-established and provides readily available labels for both depth and segmentation tasks. To show the effect of multi-task training, we first train single-task baselines (only segmentation, only depth). As can be seen, the multi-task model (MT) outperforms both single-task baselines on their respective tasks and provides the capability to compute all three edge consistencies required for our detection method. Adding our proposed edge-consistency loss (7) (Ours), even increases the segmentation performance slightly to 51.6%, while keeping the depth performance at a consistently high level.

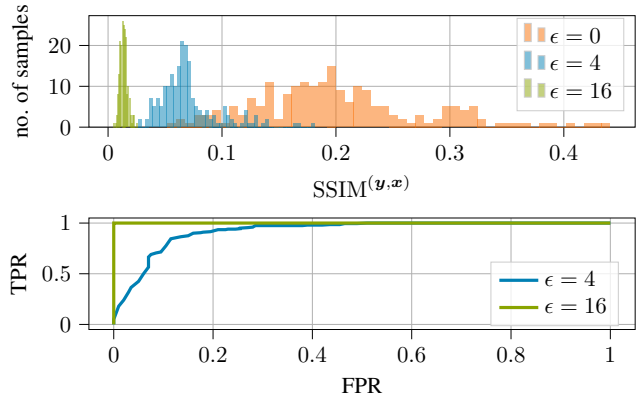
To facilitate a better detection through edge consistency, we are mainly interested in increasing the edge consistency of clean images and respective outputs ($\overline{\text{SSIM}}^{(m,x)}$, $\overline{\text{SSIM}}^{(x,d)}$, $\overline{\text{SSIM}}^{(m,d)}$), where we compute the consistency $\text{SSIM}_t^{(k,\kappa)}$ for each data sample and average over all validation set images (right hand side of Table I). We chose the SSIM metric as it does not only compare single pixel values but rather computes the similarity of image patches.

In a first experiment, we employed the commonly used smoothness loss between the depth image and the RGB image from Godard et al. [48], however, the loss does not seem to improve our edge consistency between RGB image and depth output as we observed no improvement in the $\overline{\text{SSIM}}^{(x,d)}$ metric. We therefore propose a loss function

¹We followed [25] in reporting the detection rate as it is easier to interpret compared to the F1 or AUC score and allows for a good comparison of different detectors through a common fixed false positive rate. Note that the F1 score can be obtained in straightforward fashion from the fixed false positive rate and the reported detection rate.



(a) Example image under perturbation



(b) Top: histogram over consistencies, bottom: ROC curves

Fig. 4: **Qualitative results.** We show an example image under an FGSM adversarial attack of different perturbation strengths and corresponding outputs (left). Further, we show a histogram of all samples in the KITTI-2015 validation set over the consistencies between RGB image and segmentation output under different perturbation strengths (right, top) and ROC curves for the detection performance for $\epsilon = 4$ and $\epsilon = 16$ (right, bottom).

directly enforcing the consistency w.r.t. the SSIM metric between input and both output modalities, i.e., our novel edge consistency loss (ECL) defined in (7). In the three MT + ECL experiments, we applied the loss only to *one* of the three consistencies, e.g., only to the RGB image and segmentation output in the MT + ECL(y, x) experiment. We use a rather strong weighting factor of $\mu = 0.01$ for these experiments to strongly enforce consistency. However, we observed that an improvement in one of the consistency measures usually comes at the price of a decreased consistency in another measure. The strength of this effect scales with μ but was observable in all experiments in this direction. In our full approach, we therefore apply the ECL loss on all three consistencies as described by (7) and obtain improved consistency in all three measures ($\mu = 0.003$ was optimized on the KITTI validation set), which also positively affects the detection performance, as we show in the next subsection.

B. Detection Design Ablation

Insights into our method can be gained from Fig. 4. We choose an attack design, where only the segmentation task is attacked. We later confirm that additionally attacking the depth task even improves the detection. On the left hand side, we see that the output performance decreases with increasing perturbation strength ϵ . Accordingly, the consistencies of the edges extracted from input and both outputs also decrease, as shown for the consistency between the RGB image and the segmentation output in Fig. 4, top right. We observe a distribution shift for adversarial perturbations of strength $\epsilon = 4$ and an even stronger shift for $\epsilon = 16$, indicating that with a well-chosen threshold the adversarially perturbed images can be detected. In the bottom right part of Fig. 4, we confirm this by the ROC curves of our detector under two perturbation strengths. For $\epsilon = 4$, we see that for a false positive rate (FPR) of 20% an about 90% true positive rate (i.e., detection rate) is achieved. For $\epsilon = 16$ it is even possible to choose a threshold such that the FPR is at 0% while the TPR is at 100%, i.e., a perfect detector. For all subsequent evaluations, we fix the FPR to 5% as a high FPR would generate too many

TABLE II: **Detection performance ablation** for the FGSM adversarial attack on the KITTI-2015 and Cityscapes validation sets for our proposed model (**Ours**), our model without the edge-consistency loss (w/o ECL), our model where edge consistency (10) is measured by the MAE instead of SSIM, and our model with binary edges (BE) where RGB image edges (4) and depth edges (6) are binarized by setting the top 5% gradient values to 1 and the rest to 0 (segmentation edges (9) are binary anyway). We report the detection rate $\text{TPR}_{5\%}$ [%] for various perturbation strengths as well as the average detection rate across all considered perturbation strengths. Best results on each dataset in boldface, second best underlined.

TPR _{5%}	Method	Perturbation strength ϵ						Average
		1	2	4	8	16	32	
KITTI	Ours with BE	8	<u>9</u>	12	38	<u>99</u>	100	44
	Ours with MAE	<u>6</u>	8	15	58	100	100	48
	Ours w/o ECL	8	<u>9</u>	<u>35</u>	<u>70</u>	<u>99</u>	<u>97</u>	<u>53</u>
	Ours	<u>6</u>	11	42	97	100	100	59
Cityscapes	Ours with BE	6	8	27	<u>86</u>	100	100	54
	Ours with MAE	5	11	45	100	100	100	60
	Ours w/o ECL	10	<u>27</u>	<u>82</u>	100	100	100	70
	Ours	<u>9</u>	43	100	100	100	100	75

false alarms for practical use cases.

To give more insights into our detector design, we provide several ablations in Table II. We show that our approach outperforms a model trained without our edge consistency loss (ECL), confirming that a high initial consistency on clean images benefits our detection method. We further show two variants of our detection method: First, we replace the SSIM consistency calculation with a simple mean absolute error (MAE) difference. The decreased performance of this model shows that it is important to compare the structure of the extracted edges. Second, we replaced the gradient calculation by a binary edge extraction (BE), where the top 5% gradient values are set to 1 and all other gradient values are set to 0. The worse performance of this model shows that gradient changes on a continuous scale are an important factor for our adversarial perturbation detection. These properties generalize well to the Cityscapes dataset (also assuming a 5% FPR).

Next, we are interested to see how the prediction performance of both tasks and the detection performance relate under an increasing perturbation strength ϵ , which we show in Fig. 5. We observe that while the prediction performance

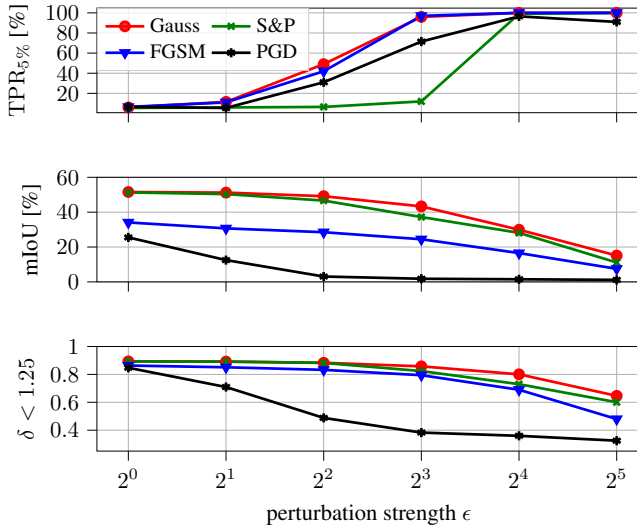


Fig. 5: **Detection performance** measured by detection rate $TPR_{5\%}$ and **prediction performance** for semantic segmentation and depth estimation measured by the mIoU and the $\delta < 1.25$ metric, respectively, for different perturbation types and strengths ϵ on the KITTI-2015 validation set.

TABLE III: **Detection performance of our method across various perturbation types** on the KITTI-2015 and Cityscapes validation sets. We report the detection rate $TPR_{5\%}$ [%] for various perturbation strengths ϵ as well as the average detection rate across all considered perturbation strengths. $TPR_{5\%} \geq 90\%$ are printed in boldface.

TPR _{5%}	Perturbation type	Perturbation strength ϵ					
		1	2	4	8	16	32
KITTI	Gaussian noise	6	12	49	96	100	100
	S & P noise	5	6	6	12	99	100
	FGSM [17]	6	11	42	97	100	100
	BIM [18]	6	7	28	74	98	99
	PGD [23]	6	5	31	71	96	91
	O-PGD [41]	6	9	26	62	99	100
Cityscapes	Gaussian noise	11	49	99	100	100	100
	S & P noise	4	4	11	65	100	100
	FGSM [17]	9	43	100	100	100	100
	BIM [18]	10	38	86	99	100	100
	PGD [23]	10	37	85	100	100	99
	O-PGD [41]	11	37	89	100	100	100

of both tasks decreases, the detection rate increases, which is the desired behavior. However, there are still some edge cases (e.g., the PGD attack at strength $\epsilon = 4$), which can fool the network to a large degree while not being detected by our method. Still, all perturbations are reliably detected at strengths of $\epsilon \geq 8$, while smaller perturbations can be defended by more robust training methods [58]. We conclude that our method provides an upper bound $\epsilon^{\max} = 4 \dots 8$ to the perturbation strengths a network needs to be robust against. Subsequently, we show that this also holds, if the attacker has white-box knowledge of our detection method.

C. Detection Performance

We find that the detection performance generalizes well across a range of adversarial perturbations, see results for FGSM, BIM, and PGD in Table III, and generalizes well to other datasets as can be seen by the strong results on the Cityscapes dataset in Table III. In particular, our method

TABLE IV: **Multi-task attack design ablation** for the PGD adversarial attack on our method on the KITTI-2015 and Cityscapes validation sets. We attack only the segmentation task (S), the depth task (D), both tasks at once (SD). We also show an attack on both tasks (SD) and the detector by additionally enforcing edge-consistency by the ECL loss (7), where the number represents the chosen value for $\bar{\mu}$ in (13). We report the detection rate $TPR_{5\%}$ [%] for various perturbation strengths as well as the average detection rate across all considered perturbation strengths. $TPR_{5\%} \geq 90\%$ are printed in boldface.

TPR _{5%}	Method	Perturbation strength ϵ					
		1	2	4	8	16	32
KITTI	S	6	5	31	71	96	91
	D	5	5	16	64	100	100
	SD	6	6	26	74	98	93
	SD + ECL(0.01)	5	7	28	76	99	93
	SD + ECL(1)	5	8	28	77	96	94
Cityscapes	S	10	37	85	100	100	99
	D	6	23	75	100	100	100
	SD	9	39	84	100	100	99
	SD + ECL(0.01)	9	36	85	99	100	99
	SD + ECL(1)	11	38	83	99	100	100

is able to handle the strong O-PGD attack [41], which implicitly optimizes at fooling our detection method and has been shown to be capable of fooling several state-of-the-art detection methods on the image classification task.

Finally, we show the effect of variants of our adversarial attack on the detection performance in Table IV. We observe that only attacking the depth task (D) yields similar detection performance as only attacking the segmentation task (S). Attacking both tasks (SD) as outlined in (12) even improves our detection method (cf. Table III), as the quality of both outputs is strongly impaired, yielding a stronger inconsistency. Enforcing edge consistency during optimization of the adversarial perturbation via our ECL loss (SD+ECL experiments, cf. 13)) does not really affect detection performance. The reason could be that increasing the consistency between input image and network outputs, and optimizing the perturbation on the input image towards a decreased network output performance are strongly conflicting goals. We therefore conclude that even under white box knowledge, an attacker cannot easily fool our detection method.

V. CONCLUSIONS

In this paper, we presented an adversarial perturbation detection method based on multi-task perception of the two complex vision tasks semantic segmentation and depth estimation. By detecting low edge consistency between input and outputs, we achieve up to 100% detection rate on strong adversarial perturbations, while 5% clean images are wrongfully classified as perturbed. We further show that our detection method benefits from a consistency-enforcing training and that even an attacker with white-box knowledge about the model properties cannot easily fool our detection method. Since our detection method reliably handles strong perturbations, it puts a natural upper limit to a perturbation strength the network must be robust against. Future work might combine our detection method with a more robust

training or adversarial defenses to reduce the negative impact of smaller perturbations on the network’s performance.

REFERENCES

- [1] L.-C. Chen, G. Papandreou, I. Kokkinos, K. Murphy, and A. L. Yuille, “DeepLab: Semantic Image Segmentation With Deep Convolutional Nets, Atrous Convolution, and Fully Connected CRFs,” *IEEE Trans. on PAMI*, vol. 40, no. 4, pp. 834–848, Apr. 2017.
- [2] A. Dahal, E. Golab, R. Garlapati, V. Ravi Kumar, and S. Yogamani, “RoadEdgeNet: Road Edge Detection System Using Surround View Camera Images,” *Electronic Imaging*, vol. 2021, no. 17, pp. 210–1, 2021.
- [3] D. Eigen, C. Puhrsch, and R. Fergus, “Depth Map Prediction from a Single Image Using a Multi-Scale Deep Network,” in *Proc. of NIPS*, Montréal, QC, Canada, Dec. 2014, pp. 2366–2374.
- [4] C. Godard, O. Mac Aodha, M. Firman, and G. J. Brostow, “Digging Into Self-Supervised Monocular Depth Estimation,” in *Proc. of ICCV*, Seoul, Korea, Oct. 2019, pp. 3828–3838.
- [5] V. Ravi Kumar, S. A. Hiremath, M. Bach, S. Milz, C. Witt, C. Pinard, S. Yogamani, and P. Mäder, “Fisheyedistancenet: Self-supervised scale-aware distance estimation using monocular fisheye camera for autonomous driving,” in *Proc. of ICRA*, 2020, pp. 574–581.
- [6] V. Ravi Kumar, M. Klingner, S. Yogamani, M. Bach, S. Milz, T. Fingscheidt, and P. Mäder, “SVDistNet: Self-Supervised Near-Field Distance Estimation on Surround View Fisheye Cameras,” *IEEE Transactions on Intelligent Transportation Systems*, pp. 1–10, 2021.
- [7] V. Ravi Kumar, S. Yogamani, S. Milz, and P. Mäder, “FisheyeDistanceNet++: Self-Supervised Fisheye Distance Estimation with Self-Attention, Robust Loss Function and Camera View Generalization,” in *Electronic Imaging*, 2021.
- [8] V. Ravi Kumar, S. Yogamani, M. Bach, C. Witt, S. Milz, and P. Mäder, “UnRectDepthNet: Self-Supervised Monocular Depth Estimation using a Generic Framework for Handling Common Camera Distortion Models,” in *Proc. of IROS*, 2020.
- [9] R. Hazem, E. Mohamed, V. R. K. Sistu, Ganesh and, C. Eising, A. El-Sallab, and S. Yogamani, “FisheyeYOLO: Object Detection on Fisheye Cameras for Autonomous Driving,” *Proc. of NeurIPS - Workshops*, 2020.
- [10] H. Rashed, E. Mohamed, G. Sistu, V. Ravi Kumar, C. Eising, A. El-Sallab, and S. Yogamani, “Generalized Object Detection on Fisheye Cameras for Autonomous Driving: Dataset, Representations and Baseline,” in *Proc. of WACV*, 2021, pp. 2272–2280.
- [11] M. Uricar, G. Sistu, H. Rashed, A. Vobecky, V. Ravi Kumar, P. Krizek, F. Burger, and S. Yogamani, “Let’s Get Dirty: GAN Based Data Augmentation for Camera Lens Soiling Detection in Autonomous Driving,” in *Proc. of WACV*, 2021, pp. 766–775.
- [12] A. Das, P. Křížek, G. Sistu, F. Bürger, S. Madasamy, M. Uříčář, V. Ravi Kumar, and S. Yogamani, “TiledSoilingNet: Tile-level Soiling Detection on Automotive Surround-view Cameras Using Coverage Metric,” in *Proc. of ITSC*, 2020, pp. 1–6.
- [13] M. Yahiaoui, H. Rashed, L. Mariotti, G. Sistu, I. Clancy, L. Yahiaoui, and S. Yogamani, “FisheyeMODNet: Moving Object Detection on Surround-view Cameras for Autonomous Driving,” in *Proc. of IMVIP*, 2019.
- [14] L. Gallagher, V. R. Kumar, S. Yogamani, and J. B. McDonald, “A Hybrid Sparse-Dense Monocular SLAM System for Autonomous Driving,” in *Proc. of ECMR*, 2021, pp. 1–8.
- [15] V. Ravi Kumar, S. Milz, C. Witt, and S. Yogamani, “Near-field Depth Estimation Using Monocular Fisheye Camera: A Semi-Supervised Learning Approach Using Sparse LiDAR Data,” in *Proc. of CVPR - Workshops*, vol. 7, 2018.
- [16] V. R. Kumar, S. Milz, C. Witt, M. Simon, K. Amende, J. Petzold, S. Yogamani, and T. Pech, “Monocular Fisheye Camera Depth Estimation Using Sparse Lidar Supervision,” in *Proc. of ITSC*, 2018, pp. 2853–2858.
- [17] I. Goodfellow, J. Shlens, and C. Szegedy, “Explaining and Harnessing Adversarial Examples,” in *Proc. of ICLR*, San Diego, CA, USA, May 2015, pp. 1–10.
- [18] A. Kurakin, I. Goodfellow, and S. Bengio, “Adversarial Examples in the Physical World,” in *Proc. of ICLR - Workshops*, Toulon, France, Apr. 2017, pp. 1–14.
- [19] S.-M. Moosavi-Dezfooli, A. Fawzi, O. Fawzi, and P. Frossard, “Universal Adversarial Perturbations,” in *Proc. of CVPR*, Honolulu, HI, USA, July 2017, pp. 1765–1773.
- [20] A. S. Hashemi, A. Bär, S. Mozaffari, and T. Fingscheidt, “Transferable Universal Adversarial Perturbations Using Generative Models,” *arXiv*, no. 2010.14919, pp. 1–9, Oct. 2020.
- [21] A. Bär, J. Löhdefink, N. Kapoor, S. J. Varghese, F. Hüger, P. Schlicht, and T. Fingscheidt, “The Vulnerability of Semantic Segmentation Networks to Adversarial Attacks in Autonomous Driving: Enhancing Extensive Environment Sensing,” *IEEE Signal Processing Magazine*, vol. 38, no. 1, pp. 42–52, Jan. 2021.
- [22] D. Hendrycks, M. Mazeika, S. Kadavath, and D. Song, “Using Self-Supervised Learning Can Improve Model Robustness and Uncertainty,” in *Proc. of NeurIPS*, Vancouver, BC, Canada, Dec. 2019, pp. 15 637–15 648.
- [23] A. Madry, A. Makelov, L. Schmidt, D. Tsipras, and A. Vladu, “Towards Deep Learning Models Resistant to Adversarial Attacks,” in *Proc. of ICLR*, Vancouver, BC, Canada, Apr. 2018, pp. 1–28.
- [24] A. Athalye, N. Carlini, and D. Wagner, “Obfuscated Gradients Give a False Sense of Security: Circumventing Defenses to Adversarial Examples,” in *Proc. of ICML*, Stockholm, Sweden, July 2018, pp. 274–283.
- [25] J. Liu, W. Zhang, Y. Zhang, D. Hou, Y. Liu, H. Zha, and N. Yu, “Detection Based Defense Against Adversarial Examples from the Steganalysis Point of View,” in *Proc. of CVPR*, Long Beach, CA, USA, June 2019, pp. 4825–4834.
- [26] J. Tian, J. Zhou, Y. Li, and J. Duan, “Detecting Adversarial Examples from Sensitivity Inconsistency of Spatial-Transform Domain,” in *Proc. of AAAI*, Virtual, Feb. 2021, pp. 1–9.
- [27] P. Sperl, C.-Y. Kao, P. Chen, X. Lei, and K. Böttinger, “DLA: Dense-Layer-Analysis for Adversarial Example Detection,” in *Proc. of EuroS&P*, Virtual, Sept. 2020, pp. 198–215.
- [28] A. Bär, M. Klingner, S. Varghese, F. Hüger, P. Schlicht, and T. Fingscheidt, “Robust Semantic Segmentation by Redundant Networks With a Layer-Specific Loss Contribution and Majority Vote,” in *Proc. of CVPR - Workshops*, Seattle, WA, USA, June 2020, pp. 1348–1358.
- [29] C. Mao, A. Gupta, V. Nitin, B. Ray, S. Song, J. Yang, and C. Vondrick, “Multitask Learning Strengthens Adversarial Robustness,” in *Proc. of ECCV*, Virtual, Aug. 2020, pp. 158–174.
- [30] A. Kendall, Y. Gal, and R. Cipolla, “Multi-Task Learning Using Uncertainty to Weigh Losses for Scene Geometry and Semantics,” in *Proc. of CVPR*, Salt Lake City, UT, USA, June 2018, pp. 7482–7491.
- [31] M. Klingner, A. Bär, and T. Fingscheidt, “Improved Noise and Attack Robustness for Semantic Segmentation by Using Multi-Task Training with Self-Supervised Depth Estimation,” in *Proc. of CVPR - Workshops*, Seattle, WA, USA, June 2020, pp. 1299–1309.
- [32] D. Wang, C. Li, S. Wen, S. Nepal, and Y. Xiang, “Defending Against Adversarial Attack Towards Deep Neural Networks via Collaborative Multi-Task Training,” *IEEE Trans. on DSCM*, pp. 1–12, 2020.
- [33] Sobh, Ibrahim and Hamed, Ahmed and Ravi Kumar, Varun and Yogamani, Senthil, “Adversarial Attacks on Multi-task Visual Perception for Autonomous Driving,” *Journal of Imaging Science and Technology*, vol. 65, no. 6, pp. 60408–1, Nov. 2021.
- [34] V. Ravi Kumar, S. Yogamani, H. Rashed, G. Sitsu, C. Witt, I. Leang, S. Milz, and P. Mäder, “Omnidet: Surround View Cameras Based Multi-Task Visual Perception Network for Autonomous Driving,” *IEEE Robotics and Automation Letters*, vol. 6, no. 2, pp. 2830–2837, 2021.
- [35] V. Ravi Kumar, M. Klingner, S. Yogamani, S. Milz, T. Fingscheidt, and P. Mäder, “SynDistNet: Self-Supervised Monocular Fisheye Camera Distance Estimation Synergized with Semantic Segmentation for Autonomous Driving,” in *Proc. of WACV*, Waikoloa, HI, USA, Jan. 2021, pp. 61–71.
- [36] S. Ghamizi, M. Cordy, M. Papadakis, and Y. L. Traon, “Adversarial Robustness in Multi-Task Learning: Promises and Illusions,” *ArXiv*, no. 2110.15053, pp. 1–9, Oct. 2021.
- [37] N. K. Gurulingan, E. Arani, and B. Zonooz, “UniNet: A Unified Scene Understanding Network and Exploring Multi-Task Relationships through the Lens of Adversarial Attacks,” in *Proc. of ICCV - Workshops*, Virtual, Oct. 2021, pp. 2239–2248.
- [38] P. Haleta, D. Likhomanov, and O. Sokol, “Multitask Adversarial Attack With Dispersion Amplification,” *EURASIP Journal on Information Security*, no. 10, pp. 1–10, 2021.
- [39] P.-Y. Chen, A. H. Liu, Y.-C. Liu, and Y.-C. F. Wang, “Towards Scene Understanding: Unsupervised Monocular Depth Estimation With Semantic-Aware Representation,” in *Proc. of CVPR*, Long Beach, CA, USA, June 2019, pp. 2624–2632.

- [40] S. Zhu, G. Brazil, and X. Liu, “The Edge of Depth: Explicit Constraints between Segmentation and Depth,” in *Proc. of CVPR*, Seattle, WA, USA, June 2020, pp. 13 116–13 125.
- [41] O. Bryniarski, N. Hingun, P. Pachuca, V. Wang, and N. Carlini, “Evading Adversarial Example Detection Defenses with Orthogonal Projected Gradient Descent,” in *Proc. of ICLR*, Virtual, Apr. 2022, pp. 1–12.
- [42] Y. Ganin and V. Lempitsky, “Unsupervised Domain Adaptation by Backpropagation,” in *Proc. of ICML*, Lille, France, July 2015, pp. 1180–1189.
- [43] M. Klingner, J.-A. Termöhlen, J. Mikolajczyk, and T. Fingscheidt, “Self-Supervised Monocular Depth Estimation: Solving the Dynamic Object Problem by Semantic Guidance,” in *Proc. of ECCV*, Glasgow, UK, Aug. 2020, pp. 582–600.
- [44] A. Paszke, A. Chaurasia, S. Kim, and E. Culurciello, “ENet: A Deep Neural Network Architecture for Real-Time Semantic Segmentation,” *arXiv*, no. 1606.02147, June 2016.
- [45] T. Zhou, M. Brown, N. Snavely, and D. G. Lowe, “Unsupervised Learning of Depth and Ego-Motion from Video,” in *Proc. of CVPR*, Honolulu, HI, USA, July 2017, pp. 1851–1860.
- [46] V. Casser, S. Pirk, R. Mahjourian, and A. Angelova, “Depth Prediction Without the Sensors: Leveraging Structure for Unsupervised Learning from Monocular Videos,” in *Proc. of AAAI*, Honolulu, HI, USA, Jan. 2019, pp. 8001–8008.
- [47] Z. Wang, A. C. Bovik, H. R. Sheikh, and E. P. Simoncelli, “Image Quality Assessment: From Error Visibility to Structural Similarity,” *IEEE Trans. Image Process.*, vol. 13, no. 4, pp. 600–612, Apr. 2004.
- [48] C. Godard, O. Mac Aodha, and G. J. Brostow, “Unsupervised Monocular Depth Estimation With Left-Right Consistency,” in *Proc. of CVPR*, Honolulu, HI, USA, July 2017, pp. 270–279.
- [49] Z. Yang, P. Wang, Y. Wang, W. Xu, and R. Nevatia, “Every Pixel Counts: Unsupervised Geometry Learning With Holistic 3D Motion Understanding,” in *Proc. of ECCV - Workshops*, Munich, Germany, Sept. 2018, pp. 1–17.
- [50] L. Liu, G. Zhai, W. Ye, and Y. Liu, “Unsupervised Learning of Scene Flow Estimation Fusing With Local Rigidity,” in *Proc. of IJCAI*, Macao, China, Aug. 2019, pp. 876–882.
- [51] A. Paszke, S. Gross, F. Massa, A. Lerer, J. Bradbury, G. Chanan, T. Killeen, Z. Lin, N. Gimelshein, L. Antiga, A. Desmaison, *et al.*, “PyTorch: An Imperative Style, High-Performance Deep Learning Library,” in *Proc. of NeurIPS*, Vancouver, BC, Canada, Dec. 2019, pp. 8024–8035.
- [52] A. Geiger, P. Lenz, C. Stiller, and R. Urtasun, “Vision Meets Robotics: The KITTI Dataset,” *International Journal of Robotics Research (IJRR)*, vol. 32, no. 11, pp. 1231–1237, Aug. 2013.
- [53] M. Cordts, M. Omran, S. Ramos, T. Rehfeld, M. Enzweiler, R. Benenson, U. Franke, S. Roth, and B. Schiele, “The Cityscapes Dataset for Semantic Urban Scene Understanding,” in *Proc. of CVPR*, Las Vegas, NV, USA, June 2016, pp. 3213–3223.
- [54] M. Menze and A. Geiger, “Object Scene Flow for Autonomous Vehicles,” in *Proc. of CVPR*, Boston, MA, USA, June 2015, pp. 3061–3070.
- [55] M. Everingham, L. Van Gool, C. K. I. Williams, J. Winn, and A. Zisserman, “The Pascal Visual Object Classes Challenge: A Retrospective,” *International Journal of Computer Vision (IJCV)*, vol. 111, no. 1, pp. 98–136, Jan. 2015.
- [56] K. He, X. Zhang, S. Ren, and J. Sun, “Deep Residual Learning for Image Recognition,” in *Proc. of CVPR*, Las Vegas, NV, USA, June 2016, pp. 770–778.
- [57] D. P. Kingma and J. Ba, “Adam: A Method for Stochastic Optimization,” in *Proc. of ICLR*, San Diego, CA, USA, May 2015, pp. 1–15.
- [58] T. Bai, J. Luo, J. Zhao, B. Wen, and Q. Wang, “Recent Advances in Adversarial Training for Adversarial Robustness,” in *Proc. of IJCAI*, Virtual, 8 2021, pp. 4312–4321.